ACS APPLIED MATERIALS & INTERFACES

Research Article

www.acsami.org

Schematic Studies on the Structural Properties and Device Physics of All Small Molecule Ternary Photovoltaic Cells

Yu Jin Kim, Jisu Hong, and Chan Eon Park*

POSTECH Organic Electronics Laboratory, Department of Chemical Engineering, Pohang University of Science and Technology, Pohang 790-784, Republic of Korea

Supporting Information

ABSTRACT: Although the field of ternary organic solar cells has seen much progress in terms of device performance in the past few years, limited understanding has restricted further development. For example, studies of the crystalline packing structure of ternary blends have rarely been reported in the solar cell field. Consequently, we chose two ternary blends of small molecules, two fullerene derivatives (small-molecule:$PC_{71}BM$:$PC_{61}BM$ or small-molecule:$PC_{71}BM$:ICBA), to investigate crystallization behavior and interactions among the three components. The crystalline structure of the ternary active blends was characterized using various techniques such as 2D-GIWAXS and AFM, and the relationship of the observed morphologies to device performance is discussed. Furthermore, the device physics associated with the charge generation, transport, and recombination dynamics of these ternary blend systems were investigated.

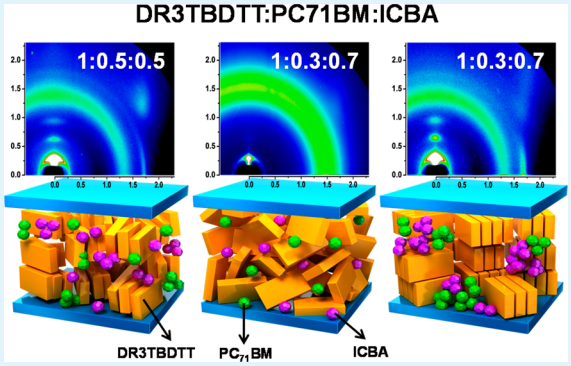

KEYWORDS: *organic solar cells, small molecule solar cells, bulk heterojunction blend, mixed acceptor, crystalline structure*

INTRODUCTION

Organic photovoltaic devices (OPVs) have various advantages, including low manufacturing costs, flexibility, and printability, and are a promising platform with which to address, in part, increasing global energy demands.[1,2] Tremendous efforts have been made to improve the power-conversion efficiency (PCE) of bulk heterojunction (BHJ) composite OPVs using various strategies, including synthesis of new active materials,[3,4] advanced device architectures,[5,6] morphology control via processing solvents,[7] and incorporating small compounds such as metallic nanoparticles and cascade materials into the active layer.[8,9] These efforts have increased our understanding of OPVs and improved PCE values to 10−11%.[10,11]

Among the promising device configurations, a ternary blend for the active layer is one of the best strategies for enhancing the performance of OPVs while retaining the simplicity of a single step for processing the absorber layer (active layer).[12,13] Most ternary blend systems in recent reports have featured two donor materials and one fullerene acceptor.[14−16] On the other hand, only a few studies have reported ternary systems based on one donor material and two fullerene acceptors. Thompson, Kim, and Chu achieved efficient ternary blend solar cells by incorporating two fullerene acceptors with a donor compound. However, they focused only on enhancement of device parameters for short-circuit current density (J_{SC}) as a result of broad ranges of light absorption and tuning of the open-circuit voltage (Voc).[17−19]

The ternary active-layer morphology within the bulk heterojunction structure remains disordered and far from ideal. The nanoscale morphology is of paramount importance because ultimately device performance is governed by the need both to dissociate photogenerated excitons and to transport both carrier types to the respective electrodes.[20,21] However, the fundamental operating mechanism and variation in the morphology of ternary blends, particularly mixed two-acceptor systems, have yet to be thoroughly investigated. The crystalline behavior and miscibility of BHJ blends based on ternary systems may differ fundamentally from those of their binary-blend counterparts. Therefore, it is important to comprehensively understand and define the parameters that govern the morphological development of ternary BHJ solar cells.

To address this issue, we systematically examined ternary OPVs via incorporation of one donor compound and two fullerene acceptors, namely: 4-thiazolidinone, 5,5-[[4,8-bis[5−2-ethylhexyl]-2-thienyl]benzo[1,2-b:4,5-b]dithiophene-2,6-diyl]bis[(3,3-dioctyl[2,2:5,2-terthiophene]-5,5-diyl)-methylidyne]]bis[3-ethyl-2-thioxo-thiophene] (DR3TBDTT)[22] as a donor small molecule, and [6,6]-phenyl-C_{71}-butyric acid methyl ester ($PC_{71}BM$), [6,6]-phenyl-C_{61}-butyric acid methyl ester ($PC_{61}BM$) and indene-C[60] bisadduct (ICBA) as acceptor materials.[23−25] Grazing incidence wide-angle X-ray scattering (GIWAXS) was used in combination with atomic force microscopy (AFM) to assess the morphology of the ternary active layer, including the ordering

Received: July 15, 2015
Accepted: September 8, 2015
Published: September 8, 2015

ACS Publications © 2015 American Chemical Society

DOI: 10.1021/acsami.5b06365
ACS Appl. Mater. Interfaces 2015, 7, 21423−21432

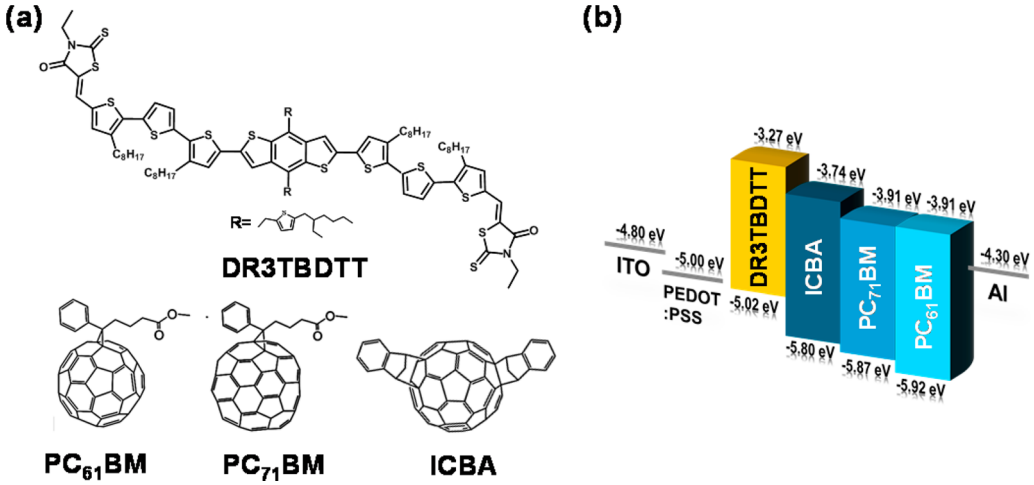

Figure 1. (a) Molecular structures of DR3TBDTT, $PC_{71}BM$, $PC_{61}BM$, and ICBA, and (b) energy band diagram of the ternary blend device.

and orientation of each component, the degree of phase separation, and the spatial distribution of each component. We correlated these morphologies with the device physics by determining the $J-V$ characteristics, charge-carrier mobility, and light-intensity analysis. In this report, we summarize what has been achieved within the framework of crystalline morphological characteristics in the field of ternary blend OPVs. To the best of our knowledge, this is the first report on how a mix of two acceptors determines the active material's crystalline properties in all-small-molecule ternary photovoltaic cells.

EXPERIMENTAL SECTION

Materials. DR3TBDTT was purchased from 1-Material, Inc. $PC_{71}BM$, $PC_{61}BM$, and ICBA were obtained from Nano-C Co., Ltd. All materials were used as received and dissolved in chloroform. All chlorinated solvents were purchased from Sigma-Aldrich.

Optical Property Measurements. The UV−vis absorption spectra were analyzed using a Cary 5000 UV−vis−NIR double-beam spectrophotometer. Background absorption was subtracted by illuminating the sample with one beam and a reference with the other beam.

Bulk Heterojunction Blend Morphology. The surface morphology of the blend active films was investigated using atomic force microscopy (AFM; Multimode IIIa, Digital Instruments) in tapping mode under ambient conditions. The measured surface area was 5 μm × 5 μm.

For structural analysis, two-dimensional GIWAXS (2D-GIWAXS) specular scans were obtained using the PLS-II3C beamlines at the Pohang Accelerator Laboratory. The 2D-GIWAXS measurements were performed using a sample-to-detector distance of 203.161 mm. The data were typically collected for 10 s using an X-ray radiation source at λ = 1.1189 nm with a 2D charge-coupled detector (CCD) (Roper Scientific, Trenton, NJ, USA). The samples were mounted on a home-built z-axis goniometer equipped with a vacuum chamber. The incidence angle a_i of the X-ray beam was set at 0.12°, an intermediate value between the critical angles of the films and the substrate ($a_{c,f}$ and $a_{c,s}$). The samples were prepared for X-ray measurements by spin-coating pure polymer and polymer blend films onto PEDOT:PSS spin-coated Si wafers.

Fabrication and Characterization of the Photovoltaic Device. Small molecule photovoltaic cells with a conventional structure of ITO/PEDOT:PSS/DR3TBDTT:fullerene derivatives ($PC_{71}BM$, $PC_{61}BM$, or ICBA) were fabricated using the following procedure. Indium tin oxide (ITO)-coated glass substrates were scrubbed with detergent, distilled water, acetone, and isopropyl alcohol for 10 min, respectively, in an ultrasonic bath. Poly(3,4-ethylene dioxythiophene):poly(styrenesulfonate) (PEDOT:PSS, Clevios P VP AI 4083) was spin-coated onto the cleaned ITO substrates at 4000 rpm for 60 s, and then thermally annealed at 120 °C for 20 min. To deposit the active layer, blend solutions of DR3TBDTT (1 wt %):acceptor compound (1 wt %) dissolved in chloroform were spin-cast on top of the electron-blocking layer (PEDOT:PSS layer) in a nitrogen-filled glovebox. Subsequently, a LiF (0.5 nm) and Al (100 nm) electrode was deposited on top of the active layer under high vacuum (2×10^{-6} Torr) by thermal evaporation. There were eight devices per substrate, with an active area of 9 mm^2 per device. Device characterization was performed under AM 1.5G irradiation with an intensity of 100 mW cm^{-2} (Oriel xenon lamp, 450 W) calibrated by a National Renewable Energy Laboratory (NREL) certified standard silicon cell. $J-V$ curves were recorded using a Keithley 2400 digital source meter. For the light-intensity-dependence measurements, AM 1.5 sunlight from a filtered xenon lamp was adjusted using a set of neutral-density filters. The external quantum efficiency (EQE) spectra were obtained using a photomodulation spectroscopic setup (model Merlin, Oriel Instruments), a calibrated Si UV detector, and an SR570 low-noise current amplifier.

Charge Carrier Mobility. For charge carrier (hole and electron) mobility measurements, a hole-only device was fabricated using the method used to fabricate the photovoltaic device, except for the cathode electrode. Therefore, the structure of the hole-only device was ITO/PEDOT:PSS/active layer/Au, with a gold electrode (Au, 100 nm) vacuum-deposited on the active layer as the cathode. The electron-only device was fabricated with an Al/active layer/Al architecture. The bottom Al layer was for electron extraction and the top of the Al layer was an electron-injecting electrode. The mobilities were determined using the Mott−Gurney relationship (space charge limited current, SCLC) to fit the current−voltage curves in the range from 0 to 4 V:

$$J = \frac{9}{8}\varepsilon_0\varepsilon_r\mu_h\frac{(V_{appl} - V_r - V_{bi})^2}{L^3}\exp\left(\beta\sqrt{\frac{V_{appl} - V_r - V_{bi}}{L}}\right)$$

where J represents the current density, L represents the film thickness of the active layer, μ_h represents the hole mobility, $\varepsilon_0\varepsilon_r$ represents the dielectric permittivity of the active layer, V_{appl} is the applied voltage, V_r represents the voltage drop due to the contact resistance and the series resistance across the electrodes, V_{bi} is the built-in voltage, and β is the field activation factor.

RESULTS AND DISCUSSION

The molecular structures of DR3TBDTT, $PC_{71}BM$, $PC_{61}BM$, and ICBA, which were the focus of this study, are shown in Figure 1a. We explored the crystallization behavior of DR3TBDTT to systematically examine the structural morpho-

DOI: 10.1021/acsami.5b06365
ACS Appl. Mater. Interfaces 2015, 7, 21423−21432

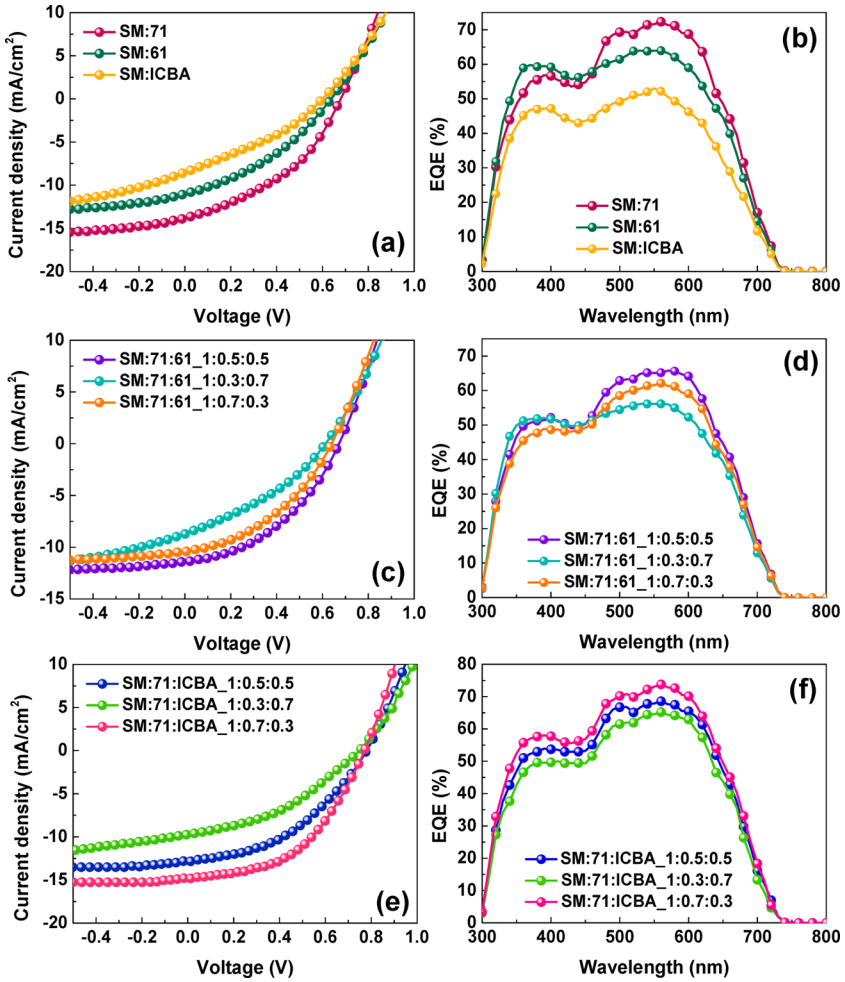

Figure 2. Current (J) versus voltage (V) characteristics of conventional OPVs with a device architecture of ITO/PEDOT:PSS/active layer/LiF/Al: (a) small molecule:single fullerene derivative, (c) small molecule:$PC_{71}BM$:$PC_{61}BM$, and (e) small molecule:$PC_{71}BM$:ICBA. External quantum efficiency (EQE) curves of the corresponding cells (b, d, and f).

Table 1. Photovoltaic Performance of Small Molecule:Single Fullerene Derivative Devices under the Same Optimized Conditions[a]

active layer	Voc (V)	Jsc (mA/cm^2)	FF (%)	PCE (%)	R_s (kΩ/cm^2)	R_{sh} (Ω/cm^2)
SM:$PC_{71}BM$	0.67 ± 0.01	13.8 ± 0.2	36.9 ± 0.05	3.45 ± 0.1	2.13 ± 0.28	745 ± 6
SM:$PC_{61}BM$	0.64 ± 0.06	10.3 ± 0.1	35.2 ± 0.1	2.31 ± 0.3	2.75 ± 0.14	730 ± 3
SM:ICBA	0.61 ± 0.01	6.78 ± 0.32	30.2 ± 0.7	1.19 ± 0.3	3.12 ± 0.21	547 ± 5

[a]Average data from 20 devices.

logical characteristics of a ternary blend model system using different fullerene derivatives. Furthermore, the DR3TBDTT compound is a novel small molecule with a PCE value of 8.12%;[22] thus, this research using the DR3TBDTT is quite meaningful work. In terms of alignment of energy levels, the appropriate energy levels of three fullerene derivatives, positioned to that of DR3TBDTT, form a cascade energy level structure that facilitates exciton dissociation and provides more routes for charge transfer (Figure 1b).[26]

Application to Small Molecule Photovoltaic Cells. The $PC_{71}BM$:$PC_{61}BM$ or $PC_{71}BM$:ICBA fullerene composition had a significant influence on overall solar cell performance in all of the investigated systems. Figure 2a,c,e presents the current density versus voltage (J–V) characteristics of the best photovoltaics with regular structures, ITO/PEDOT:PSS/active layer/LiF/Al, under 100 W m^{-2} air mass and 1.5 G illumination. Device parameters such as open-circuit voltage (Voc), short-circuit current (Jsc), fill factor (FF), and PCE values were deduced from the J–V curves (summarized to average values in Tables 1–3). To maximize the effects of the morphologically crystalline structure by mixing components in heterojunction blend films, we used the same optimized conditions for all photovoltaic devices: a donor:acceptor stoichiometry of 1:1 w/w, a 20 mg/mL total blend solution, and an active layer thickness in the range 92–95 nm. Initially, the device performance of the binary (DR3TBDTT:single fullerene derivative) BHJ solar cells was characterized by a Voc value of 0.67 V, a J_{SC} value of 13.8 mA cm^{-2}, and an FF value of 36.9%, corresponding to a PCE value of 3.45% in the DR3TBDTT:$PC_{71}BM$ (SM:71) devices, which had the highest performance among the DR3TBDTT:single fullerene derivative devices (PCE values of 2.31% for DR3TBDTT:$PC_{61}BM$

DOI: 10.1021/acsami.5b06365
ACS Appl. Mater. Interfaces 2015, 7, 21423–21432

Table 2. Efficiency Parameters of Solar Cells Based on SM:$PC_{71}BM$:$PC_{61}BM$ with Different Blend Ratios[a]

active layer	Voc (V)	Jsc (mA/cm^2)	FF (%)	PCE (%)	R_s (kΩ/cm^2)	R_{sh} (Ω/cm^2)
SM:71:61_1:0.5:0.5	0.67 ± 0.02	10.5 ± 0.2	42.5 ± 0.2	3.04 ± 0.2	2.05 ± 0.3	658 ± 7
SM:71:61_1:0.3:0.7	0.62 ± 0.01	7.8 ± 0.26	33.8 ± 0.13	1.63 ± 0.2	3.95 ± 0.25	521 ± 4
SM:71:61_1:0.7:0.3	0.62 ± 0.03	10.2 ± 0.16	41.8 ± 0.3	2.52 ± 0.1	2.61 ± 0.27	567 ± 4

[a]Average data from 20 devices.

Table 3. Photovoltaic Performance of the SM:$PC_{71}BM$:ICBA in Standard BHJ Devices with Various Donor:Acceptor:Acceptor Blend Ratios[a]

active layer	Voc (V)	Jsc (mA/cm^2)	FF (%)	PCE (%)	R_s (kΩ/cm^2)	R_{sh} (Ω/cm^2)
SM:71:ICBA_1:0.5:0.5	0.77 ± 0.01	12.2 ± 0.2	44.3 ± 0.1	4.18 ± 0.2	1.84 ± 0.14	728 ± 3
SM:71:ICBA_1:0.3:0.7	0.73 ± 0.02	9.8 ± 0.2	41.2 ± 0.23	2.93 ± 0.1	2.22 ± 0.26	703 ± 2
SM:71:ICBA_1:0.7:0.3	0.76 ± 0.01	14.2 ± 0.3	47.1 ± 0.05	5.11 ± 0.2	1.31 ± 0.22	892 ± 5

[a]"avg" is the photovoltaic parameters of 20 solar cells with the average PCEs.

(SM:61) and 1.19% for DR3TBDTT:ICBA (SM:ICBA)). As discussed below, the significant differences in photovoltaic performance are thought to have been due to the considerable differences in the photocurrent values that dominantly result from the various structural packing morphologies (Because exciton generation value is considerably similar to 8.56×10^{27} m^{-3} s^{-1}, 8.34×10^{27} m^{-3} s^{-1}, and 8.38×10^{27} m^{-3} s^{-1} for the SM:71, SM:61, and SM:ICBA system, respectively). First, we can simply expect for structural packing morphologies that the SM:71 films have more molecular interchain interactions and enhanced local structural order than two other films by UV−vis absorption data (Supporting Information).[27,28] When incorporating the $PC_{61}BM$ compound into the DR3TBDTT:$PC_{71}BM$ blends, the PCE showed different aspects depending on the $PC_{71}BM$:$PC_{61}BM$ blend ratio (see Table 2). A PCE value of 3.04% was obtained using the composition DR3TBDTT:$PC_{71}BM$:$PC_{61}BM$ (SM:71:61) = 1:0.5:0.5, resulting in a *Voc* value of 0.67 V, a J_{SC} value of 10.5 mA cm^{-2}, and an value FF of 42.5%. More interesting than the results for DR3TBDTT:$PC_{71}BM$:$PC_{61}BM$, however, was the DR3TBDTT:$PC_{71}BM$:ICBA (SM:71:ICBA) ternary model system. The device parameters increased remarkably under all fullerene blend conditions in comparison with the DR3TBDTT:single fullerene derivative and DR3TBDTT:$PC_{71}BM$:$PC_{61}BM$ blends. In DR3TBDTT:$PC_{71}BM$:ICBA with 1:0.5:0.5 and 1:0.3:0.7 blend ratios, we observed PCE values of 4.18% and 2.93%, respectively, whereas a PCE value of 5.11%, a *Voc* value of 0.76 V, a J_{SC} value of 14.2 mA cm^{-2}, and an FF value of 47.1% were achieved in the DR3TBDTT:$PC_{71}BM$:ICBA = 1:0.7:0.3 device (these parameters were the highest values among all photovoltaic device results). These results suggest that the addition of various amounts ICBA not only led to morphological variation but also suppressed gemination- and/or nongeminate recombination, as will be discussed below.

The EQE spectra at a given wavelength reflect the light response of a device and are related directly to the value of the photocurrent density, J_{SC}.[29,30] The EQE spectra of the binary and ternary devices in Figure 2b,d,f reveal photocurrent responses in the 300−800 nm wavelength range. The EQE results agree very well with the J_{SC} values mentioned above.

Surface Morphological Properties of BHJ Active Layers. The AFM images provide clear nanoscale morphological information for all of the small-molecule-blend films. Therefore, we investigated the active film morphologies of all of the binary and ternary blends by performing tapping mode AFM (see Figure 3). Correct aggregated surface and nanophase separation is responsible for the charge carrier transport

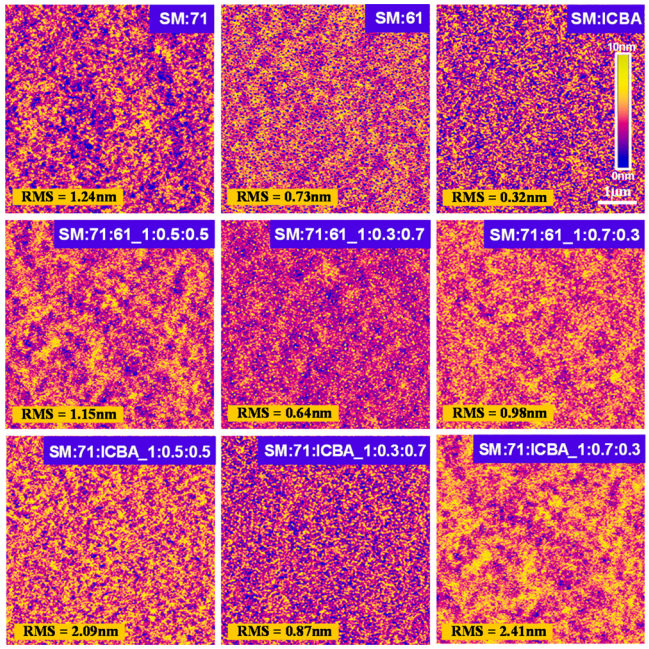

Figure 3. AFM topography of blend active films from DR3TBDTT:fullerene derivatives; first line: DR3TBDTT (SM): a single fullerene derivative, second line: DR3TBDTT:$PC_{71}BM$:$PC_{61}BM$ (SM:71:61) blends with different blend compositions, and third line: DR3TBDTT:$PC_{71}BM$:ICBA (SM:71:ICBA) films.

required to boost photocurrent density.[31] In the DR3TBDTT:single fullerene derivative films, the phase-separated and aggregated domains with root-mean-squared (RMS) roughness were slightly enhanced in the order: SM:71 (RMS = 1.24 nm) > SM:61 (RMS = 0.73 nm) > SM:ICBA (RMS = 0.32 nm). The relatively large domains and roughness of the SM:71 blend indicate that this film had reduced internal resistance and more efficient charge separation and transport in the device. Thus, these effects led to an increase in the J_{SC} and overall PCE values of the photovoltaic cell.[32] When blending DR3TBDTT:$PC_{71}BM$ with $PC_{61}BM$, two films with blend ratios of 1:0.5:0.5 and 1:0.7:0.3 exhibited segregated nanophase morphology with an aggregated pathway, whereas the SM:71:61 with 1:0.3:0.7 film showed a flat and featureless

DOI: 10.1021/acsami.5b06365
ACS Appl. Mater. Interfaces 2015, 7, 21423−21432

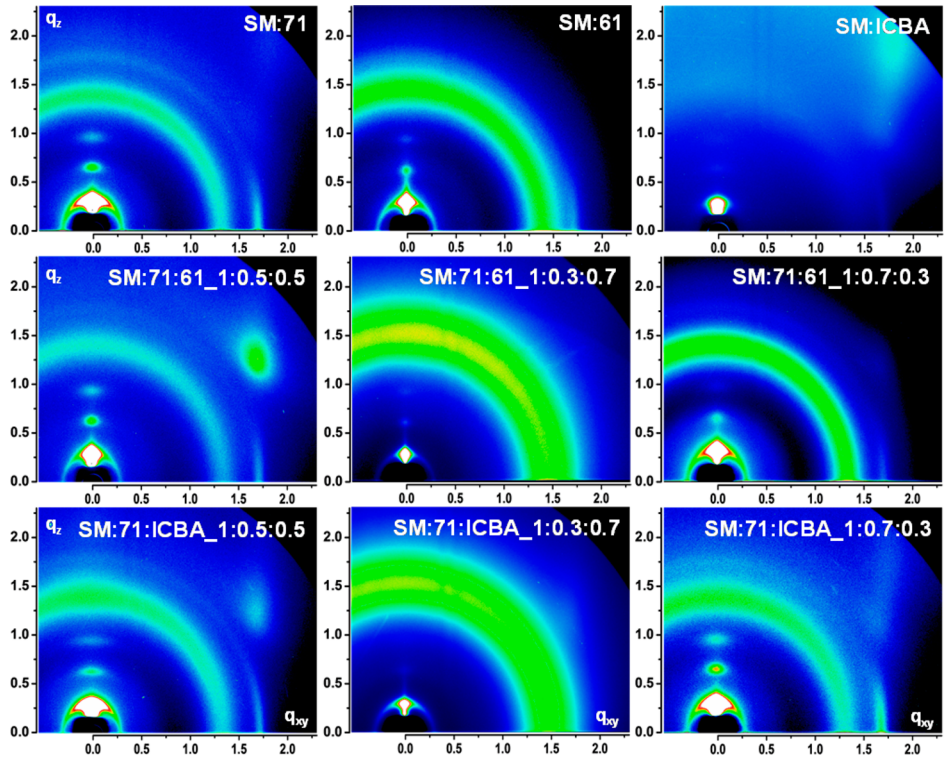

Figure 4. 2D-GIWAXS images of small-molecule (SM, DR3TBDTT):fullerene derivatives; first row shows SM:single fullerene ($PC_{71}BM$, $PC_{61}BM$, or ICBA) films, second row shows SM:$PC_{71}BM$:$PC_{61}BM$ blends processed with different blend ratios, and third row shows SM:$PC_{71}BM$:ICBA ternary films with various blend ratios.

surface with an RMS roughness of 0.64 nm. This suggests that the film with greater phase separation and a clearer segregated domain morphology originated from improvements in the intermolecular interactions of the small-molecule compounds, which allowed for efficient charge-carrier movement and improved device performance, particularly as regards J_{SC} values.[33] Likewise, with incorporation of the ICBA compound into the DR3TBDTT:$PC_{71}BM$ blend, the SM:71:ICBA = 1:0.5:0.5 and SM:71:ICBA = 1:0.7:0.3 blends showed sufficiently phase-separated domains and segregated networks with RMS roughness values of 2.09 and 2.41 nm, respectively. On the other hand, the SM:71:ICBA = 1:0.3:0.7 film had a smooth and homogeneous surface morphology. Relating the AFM results to the device data, we suggest that a more aggregated and phase-separated surface results from the enhanced intermolecular interactions of the compound, inducing efficient charge carrier transport and generating a greater photocurrent in DR3TBDTT:fullerene derivative systems.

Structural Study Using Grazing Incidence X-ray Scattering. The AFM results did not clearly show the blends' morphological characteristics. Therefore, to inspect the molecular organization in the bulk morphology phases and correlate these structural studies with device performance, 2D-GIWAXS of the binary and ternary blended layers was performed and the films were compared (Figure 4). Before defining the variation in crystalline structure as a result of mixed fullerene acceptors in the BHJ active layer, we performed a 2D-GIWAXS analysis of pure DR3TBDTT, $PC_{71}BM$, $PC_{61}BM$, and ICBA films (Figure S2). The DR3TBDTT film produced scattered strong (h00) diffraction peaks ($q_{z_{(100)}} \approx 0.32$ Å^{-1}) in the out-of plane direction, with a clear (010) reflection peak ($q_{xy} \approx 1.69$ Å^{-1}) in the in-plane direction, which is consistent with previous results.[22] Furthermore, all three fullerene derivative films exhibited an isotropic broad scattering peak, indicative of random aggregation in the fullerene derivative compound domains.[34] In the case of the DR3TBDTT:single fullerene derivative, the 2D-GIWAXS pattern of the SM:71 film produced distinct and strong scattering peaks originating from the crystalline domains of the DR3TBDTT compound in both out-of plane and in-plane directions. The SM:61 blend produced only second-order peaks in the out-of plane direction and a weak $\pi-\pi$ stacking peak in the in-plane direction (see Figure S3, the scattering linecuts extracted from 2D-GIWAXS images), suggesting that the crystallinity of the DR3TBDTT molecules with molecular packing order was signficantly reduced with an edge-on manner in SM:61 blends compared to SM:71films.[35] Surprisingly, none of the peaks observed for the SM:ICBA blended film appeared in the 2D-GIWAXS image, which is indicative of a random orientation of the DR3TBDTT molecules.[35] These results are consistent with the trends of the AFM data, and we argue that the aggregated domains are due to the crystalline packing domains of the DR3TBDTT compounds. Furthermore, we propose that the greater the crystallinity of the DR3TBDTT molecules with an ordered packing system in the active blend films, the better the device performance achieved. In other words, the enhanced structural order may function as an important factor in higher photocurrent density and lead to improved device performance. This trend was also observed in DR3TBDTT:PC_{71}B-M:$PC_{61}BM$ and DR3TBDTT:$PC_{71}BM$:ICBA. In the ternary blended films, the 2D-GIWAXS patterns of both SM:71:61 and SM:71:ICBA BHJs with 1:0.3:0.7 compositional ratios had only broad halo peaks with no distinct reflection peaks, suggestive of an intermixed blend of the three compounds.[36] Interestingly, increased structural order with stronger scattering intensity

DOI: 10.1021/acsami.5b06365
ACS Appl. Mater. Interfaces 2015, 7, 21423−21432

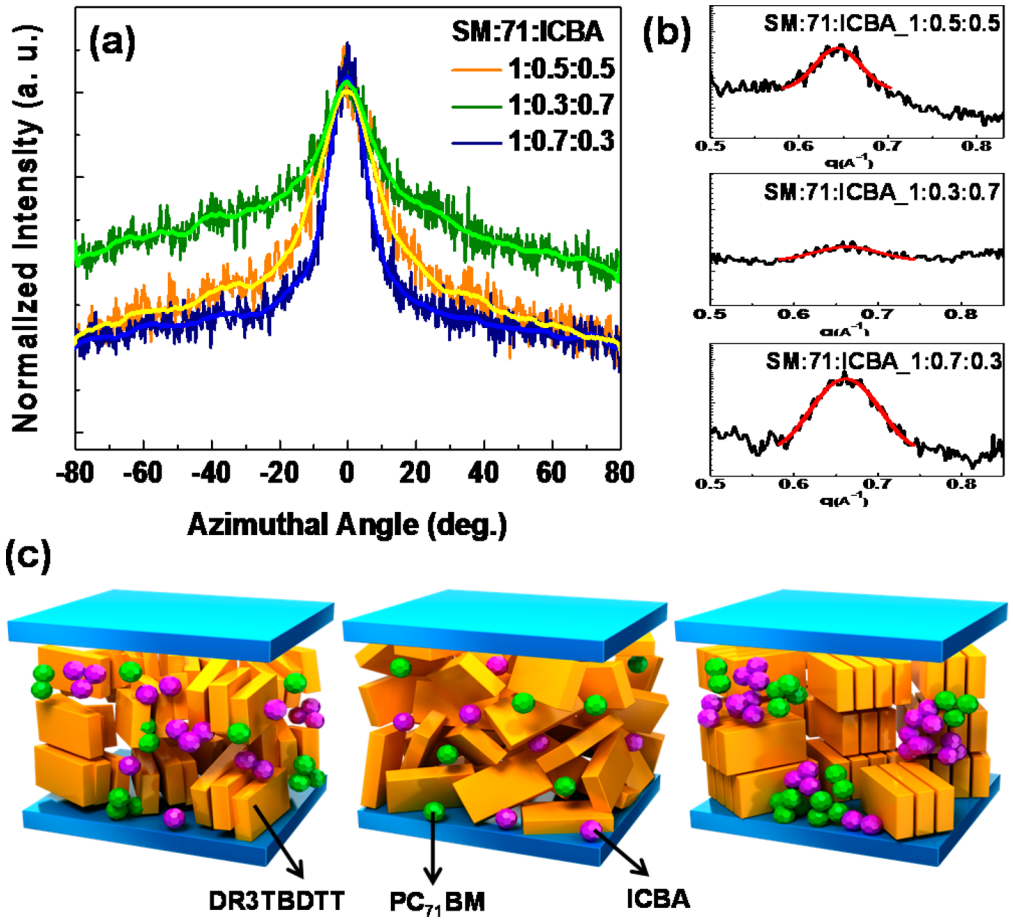

Figure 5. (a) Azimuthal line scans for a (200) peak in SM:PC_{71}BM:ICBA blend films. (b) Three fitting curves in the (200) peak position of out-of scattering profiles were extracted using the Gauss model (fwhm =0.08, 0.14, and 0.05 for 1:0.5:0.5, 1:0.3:0.7, and 1:0.7:0.3 blend ratio films, respectively). (c) Proposed schematic illustration of the dominant transformations of the DR3TBDTT:PC_{71}BM:ICBA ternary blend morphology (1:0.5:0.5, 1:0.3:0.7, and 1:0.7:0.3 in the sequence).

appeared in the 2D-GIWAXS patterns in the sequence: 1:0.5:0.5 > 1:0.7:0.3 blend ratios for SM:71:61 films and 1:0.7:0.3 > 1:0.5:0.5 weight ratios for SM:71:ICBA films.

To summarize the 2D-GIWAXS results, the crystalline structure of the DR3TBDTT compound changed significantly in the blended systems composed of different fullerene derivatives: DR3TBDTT crystalline domains packed in a more orderly manner resulted in high J_{SC} values. For these reasons, we observed enhanced performance for DR3TBDTT:PC_{71}BM:ICBA (1:0.7:0.3) devices.

To elucidate the association between the crystallinity of DR3TBDTT and device performance in DR3TBDTT:PC_{71}BM:ICBA blends, we investigated detailed structural evolution through crystalline orientation and crystal size analysis (Figure 5). Estimation of DR3TBDTT crystallinity from the (200) reflections has to include the azimuthal distribution that accounts for differently oriented crystallites. The azimuthal distribution of (200) reflection intensity is shown in Figure 5a. Indeed, comparison of the azimuthal angular breadths of the DR3TBDTT (200) peaks shows a clear difference between samples with different blend ratios. It can be seen that the degree of crystal orientation with edge-on orientation on the surface increases in the order: 1:0.7:0.3 > 1:0.5:0.5 > 1:0.3:0.7 weight ratio films. This suggests that the higher crystalline orientation of DR3TBDTT improves hole transport in DR3TBDTT domains, leading to an enhanced charge transport balance between holes and electrons, thereby elevating current density and the fill factor.[37,38]

To obtain further quantitative structural information on DR3TBDTT ordered perpendicular to the substrate, we calculated the DR3TBDTT crystallite size deduced from the full width at half-maximum (fwhm) of a (200) interlamellar peak (the (200) peak position and fwhm were extracted by Gauss fitting, shown in Figure 5b). The sizes of the DR3TBDTT crystalline domains formed in the DR3TBDTT:PC_{71}BM:ICBA blend can be obtained from the Scherrer equation:[39]

$$\tau = \frac{K\lambda}{\beta \cos\theta}$$

where τ is the mean size of the ordered crystalline domains, K is a dimensionless shape factor (that has a typical value of about 0.9), λ is the X-ray wavelength, β is the line broadening at the fwhm, and θ is the Bragg angle. Using Scherrer's formula, the average DR3TBDTT crystallite size (τ) gradually increased in the order 122.5 Å (1:0.7:0.3), 76.6 Å (1:0.5:0.5), and 43.8 Å (1:0.3:0.7). This indicates that the 1:0.7:0.3 compositional ratio in DR3TBDTT:PC_{71}BM:ICBA blends induces not only an increase in the mean size of crystallites but also well-organized crystalline DR3TBDTT domains.

The combined 2D-GIWAXS patterns and azimuthal distribution analyzed here to assess film structural morphology

DOI: 10.1021/acsami.5b06365
ACS Appl. Mater. Interfaces 2015, 7, 21423−21432

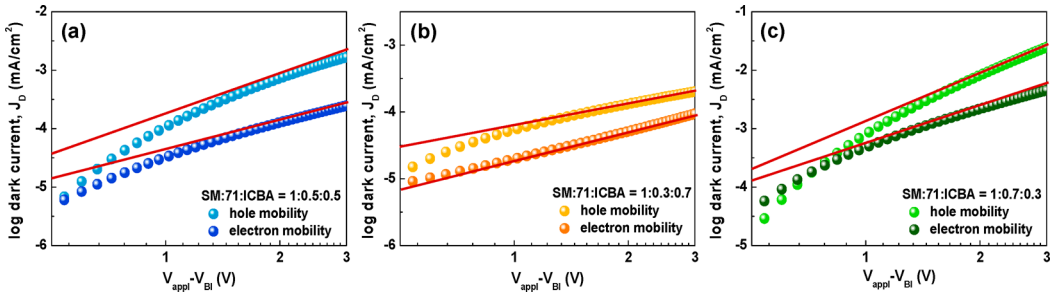

Figure 6. Dark J−V characteristics of DR3TBDTT:PC_{71}BM:ICBA devices, including hole-only devices and electron-only devices, respectively: (a) 1:0.5:0.5, (b) 1:0.3:0.7, and (c) 1:0.7:0.3.

clearly show that blend ratios are a dominant factor in determining the compound crystallites in these ternary blends, as shown in Figure 5c. As discussed above, the crystalline DR3TBDTT domains stacked more readily in an edge-on manner with a slightly broader orientation in SM:71:ICBA (1:0.5:0.5) blends than in SM:71:ICBA (1:0.3:0.7) films. However, the DR3TBDTT crystallites were remarkably well-ordered with larger crystalline domain sizes in SM:71:ICBA (1:0.7:0.3) compared with the two ternary blends. Based on the findings that the device performance of the DR3TBDTT:PC_{71}BM:ICBA = 1:0.7:0.3 system was dominantly enhanced by charge transport improvements resulting from well-organized crystalline DR3TBDTT domains, it is now possible to correlate the charge-carrier mobility to these analyses.

Charge Transport Studies. Ideally, efficient photoinduced charge generation should be followed by efficient charge extraction processes. In the case of limited carrier mobility, photogenerated carriers cannot be swept out efficiently by electrode collection before recombination.[40] Therefore, to elucidate the effects of crystalline packing structures within ternary small-molecule composites on charge transport, SCLC spectroscopy was used to map out charge-carrier mobilities in DR3TBDTT:PC_{71}BM:ICBA films. The J−V characteristics of both hole-only and electron-only diodes can be well fitted to the Mott−Gurney relation for an SCLC. As shown in Figure 6 and Table 4, fitting to the experimental results revealed that the hole mobilities were 8.54×10^{-5} cm^2 V^{-1} s^{-1} for SM:71:ICBA (1:0.3:0.7) and 4.07×10^{-4} cm^2 V^{-1} s^{-1} for SM:71:ICBA (1:0.5:0.5), almost a 2-fold difference. On the other hand, a larger increase of 7.62×10^{-4} cm^2 V^{-1} s^{-1} was observed for SM:71:ICBA (1:0.7:0.3), which implies that this higher hole carrier mobility was the result of more intermolecular interactions and molecular ordering than in the two ternary compositional blends, which is in good agreement with our expectations based on the crystallite analyses. In addition, this hole mobility trend also appears in the electron mobility results. The electron mobility of the 1:0.5:0.5, 1:0.3:0.7, and 1:0.7:0.3 blends exhibited values of 8.62×10^{-5} cm^2 V^{-1} s^{-1}, 6.21×10^{-6} cm^2 V^{-1} s^{-1}, and 5.90×10^{-4} cm^2 V^{-1} s^{-1}, respectively. The larger electron mobility of the SM:71:ICBA = 1:0.7:0.3 blend can be attributed to the crystalline characteristics of DR3TBDTT in the solid state, which induced the formation of an aggregation network between mixed acceptor domains.[41]

Table 4. Charge Mobilities in the Ternary Blend Films, DR3TBDTT:PC_{71}BM:ICBA, of Different Compositional Ratios in Hole and Electron Only Devices

SM:71:ICBA	μ_h (cm^2 /V s)	μ_e (cm^2 /V s)	μ_h/μ_e
1:0.5:0.5	4.07×10^{-4}	8.62×10^{-5}	5.34
1:0.3:0.7	8.54×10^{-5}	6.21×10^{-6}	13.75
1:0.7:0.3	7.62×10^{-4}	5.90×10^{-4}	1.29

Furthermore, a high structural order typically causes a high or balanced carrier mobility and thus impedes nongeminate recombination in devices.[42] As shown in Table 4, the hole and electron mobilities were most balanced in the SM:71:ICBA = 1:0.7:0.3 device, and perhaps represent the most important inferred properties for high device performance, particularly FF values.

Charge Generation and Recombination Dynamics. To clarify the differences in the J_{SC} values of the DR3TBDTT:PC_{71}BM:ICBA systems further, we studied the charge photogeneration of the ternary blended devices. Figure 7a shows the photocurrent density (J_{ph}) versus the effective voltage (V_{eff}) of the devices with 1:0.5:0.5, 1:0.3:0.7, and 1:0.7:0.3 blend weight ratios. The measured J_{ph} is given by $J_{ph} = J_L$ (photocurrent under illumination) $- J_D$ (photocurrent under dark) and the V_{eff} is defined by $V_{eff} = V_0$ (voltage where $J_{ph} = 0$) $- V_{appl}$ (applied bias voltage).[43] We assume that all photogenerated excitons are dissociated into free charge carriers at high V_{eff} (2 V in this case) due to a sufficient electric field.[38] Therefore, the exciton generation rate (G_{max}) can be determined from the saturation current density (J_{sat}):

$$J_{sat} = qLG_{max}$$

where q is the elementary charge and L is the thickness of the active layer.[44] From Figure 7a, the values of G_{max} for the SM:71:ICBA = 1:0.5:0.5, 1:0.3:0.7, and 1:0.7:0.3 devices are found to be 8.92×10^{27} m^{-3} s^{-1}, 8.01×10^{27} m^{-3} s^{-1}, and 9.15×10^{27} m^{-3} s^{-1}, respectively. This result suggests that there is rarely no differences of the formation of free charge carriers for excition generation by light absorption in different blend compositions. Absolutely among them, however, the slightly increased G_{max} with 1:0.7:0.3 blend ratios is suggestive of increased overall exciton generation in the ternary devices.[45] We also calculated the charge dissociation probability, $P(E,T)$ (which is determined from the ratio of J_{ph}/J_{sat}[46]), for three devices with different weight ratios. The $P(E,T)$ values of 1:0.5:0.5, 1:0.3:0.7, and 1:0.7:0.3 under short-circuit conditions were 73%, 62%, and 87%, respectively, implying that $P(E,T)$ was higher in the DR3TBDTT:PC_{71}BM:ICBA = 1:0.7:0.3 than in the other two blends, which is attributed to its improved structural nanophase morphology.

The dependence of J_{SC} and Voc values at various light intensities elucidated the influence of crystalline packing structures on recombination processes in our DR3TBDTT:PC_{71}BM:ICBA ternary system. In principle, J_{SC}

DOI: 10.1021/acsami.5b06365
ACS Appl. Mater. Interfaces 2015, 7, 21423−21432

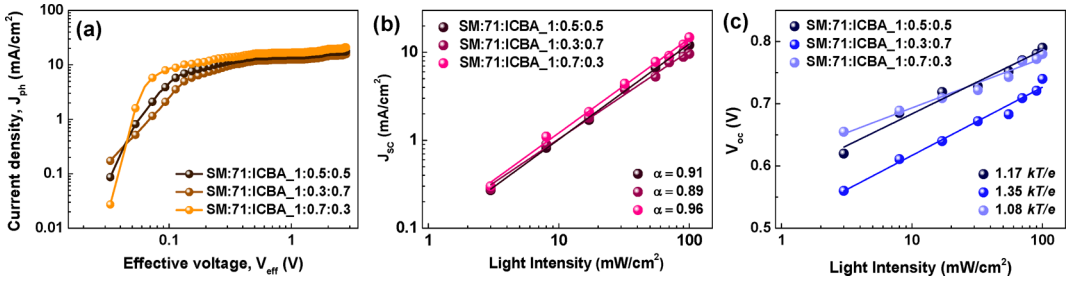

Figure 7. (a) Photocurrent density versus effective voltage (J_{ph}−V_{eff}) characteristics for three SM:PC_{71}BM:ICBA devices under constant incident light intensity. Light intensity dependence of SM:PC_{71}BM:ICBA solar cells spin-coated from blend solution with different compositional ratios: (b) J_{SC} and (c) *V*oc.

shows a power-law dependence on light intensity, which can be expressed as

$$J_{sc} = \beta(P_{light})^{\alpha}$$

where P_{light} is the light intensity, α is the exponential factor, and β is a constant value.[47] Under ideal conditions, the second-order (nongeminate) recombination should be minimized ($\alpha \approx 1$), and any deviation of α from 1 implies that second-order recombination has occurred.[46] As exhibited in Figure 7b, the extracted α values were 0.91, 0.89, and 0.96 for 1:0.5:0.5, 1:0.3:0.7, and 1:0.7:0.3 devices, respectively. The value close to unity in the SM:71:ICBA (1:0.7:0.3) device illustrates that the carrier sweep-out was the most efficient and almost suppressed second-order recombination at the built in field.[48] This is in agreement with the balanced charge transport observed in the mobility study.

Figure 7c shows the relationship between *V*oc values and light intensity in our ternary devices. Under the open-circuit condition, all photogenerated carriers recombine within the cell. Therefore, the recombination mechanism can be verified using the dependence of *V*oc on light intensity. *V*oc and light intensity are related as follows:[49]

$$V_{oc} \cong \frac{kT}{e}\ln(P_{light}) + C$$

where e is the elementary charge, k is the Boltzmann constant, T is the temperature in Kelvin, P_{light} is the light intensity, and C is a constant. The slope of thermal voltage (kT/e) shows second-order recombination as opposed to a higher slope ($2\ kT/e$), which is assigned to trap-assisted recombination.[49] In Figure 7c, the slope yields are 1.17 kT/e for the SM:71:ICBA = 1:0.5:0.5 device and 1.35 kT/e for the SM:71:ICBA = 1:0.3:0.7 device, whereas it is only 1.08 kT/e for the SM:71:ICBA = 1:0.7:0.3 device, implying that trap-assisted recombination is almost negligible in this device. Therefore, the results indicate that 1:0.7:0.3 compositional blends in DR3TBDTT:PC_{71}BM:ICBA reduced interfacial surface trap densities between the active layer materials in the devices, suppressed trap-assisted recombination, and contributed to enhanced J_{SC} values.[50]

CONCLUSION

In summary, we schematically studied the structural packing morphology of ternary blends of DR3TBDTT:two fullerene derivatives by controlling different mixed acceptors (PC_{71}BM:PC_{61}BM or PC_{71}BM:ICBA). The nanophase crystalline structures of these systems were examined in depth using 2D-GIWAXS and AFM techniques, which revealed that the more DR3TBDTT crystallite ordering was enhanced, the more device performance improved, particularly photocurrent density. Among all of the ternary DR3TBDTT:two fullerene derivative blends, the DR3TBDTT:PC_{71}BM:ICBA blend solar cell with a 1:0.7:0.3 weight ratio demonstrated the highest PCE value at 5.11%. This resulted in a near-ideal DR3TBDTT:fullerene morphology (highly crystalline, preferentially well-orientated in an edge-on manner with large compound domains), which was determined by the DR3TBDTT crystalline structure (crystallities) and was sensitive to the choice of blend ratios. In this higher crystalline ternary system, charge recombination was suppressed while charge transport was improved as a result of more effective charge generation and extraction. Therefore, we emphasize that it is possible to change the structural morphology and carrier dynamic characteristics based on the compositional blend ratios of the ternary active blend in DR3TBDTT ternary solar cell systems.

Our approach will allow the ternary solar cell community to explore all-small-molecule materials and optimize their combinations under a well-controlled morphological landscape that should greatly accelerate materials and process development toward improved ternary solar cells. Our results elucidate all-small-molecule ternary blend structures and can be used in the development of improved ternary solar cells.

ASSOCIATED CONTENT

Supporting Information

The Supporting Information is available free of charge on the ACS Publications website at DOI: 10.1021/acsami.5b06365.

UV−vis absorption spectra of binary and ternary active blends, 2D-GIWAXS patterns for pure DR3TBDTT, PC_{71}BM, PC_{61}BM, and ICBA, and out-of- and in-plane scattering profiles along the q_z and q_{xy} axes from 2D-GIWAXS images of binary- and ternary-blend films (PDF)

AUTHOR INFORMATION

Corresponding Author

*E-mail: cep@postech.ac.kr.

Notes

The authors declare no competing financial interest.

ACKNOWLEDGMENTS

This study was supported by a grant from the National Research Foundation of Korea (NRF) funded by the Korean Government (MSIP NRF-2014R1A2A1A05004993) and by a grant from the Center for Advanced Soft Electronics (2011-0031639) under the Global Frontier Research Program of the

DOI: 10.1021/acsami.5b06365
ACS Appl. Mater. Interfaces 2015, 7, 21423−21432

Ministry of Education, Science, and Technology, Korea. This research was also supported by a New & Renewable Energy of the Korea Institute of Energy Technology Evaluation and Planning (KETEP) grant funded by the Korean Government through the Ministry of Knowledge Economy (No. 20123010010140).

REFERENCES

(1) Yu, G.; Gao, J.; Hummelen, J. C.; Wudl, F.; Heeger, A. J. Polymer Photovoltaic Cells: Enhanced Efficiencies via a Network of Internal Donor-Acceptor Heterojunctions. *Science* **1995**, *270*, 1789−1791.
(2) Cheng, Y. − J.; Yang, S. − H.; Hsu, C. − S. Synthesis of Conjugated Polymers for Organic Solar Cell Applications. *Chem. Rev.* **2009**, *109*, 5868−5923.
(3) Zhang, Q.; Kan, B.; Liu, F.; Long, G.; Wan, X.; Chen, X.; Zuo, Y.; Ni, W.; Zhang, H.; Li, M.; Hu, Z.; Huang, F.; Cao, Y.; Liang, Z.; Zhang, M.; Russell, T. P.; Chen, Y. Small-molecule Solar Cells with Efficiency over 9%. *Nat. Photonics* **2014**, *9*, 35−41.
(4) Huo, L.; Liu, T.; Sun, X.; Cai, Y.; Heeger, A. J.; Sun, Y. Single-Junction Organic Solar Cells Based on a Novel Wide-Bandgap Polymer with Efficiency of 9.7%. *Adv. Mater.* **2015**, *27*, 2938−2944.
(5) Yang, Y.; Mielczarek, K.; Aryal, M.; Zakhidov, A.; Hu, W. Nanoimprinted Polymer Solar Cell. *ACS Nano* **2012**, *6*, 2877−2892.
(6) Jeong, S.; Cho, C.; Kang, H.; Kim, K. − H.; Yuk, Y.; Park, J. Y.; Kim, B. J.; Lee, J. − Y. Nanoimprinting-Induced Nanomorphological Transition in Polymer Solar Cells: Enhanced Electrical and Optical Performance. *ACS Nano* **2015**, *9*, 2773−2782.
(7) Franeker, J. J.; Turbiez, M.; Li, W.; Wienk, M. M.; Janssen, R. A. J. A Real-Time Study of the Benefits of Co-Solvents in Polymer Solar Cell Processing. *Nat. Commun.* **2015**, *6*, 6229.
(8) Choi, H.; Ko, S. − J.; Choi, Y.; Joo, P.; Kim, T.; Lee, B. R.; Jung, J. − W.; Choi, H. J.; Cha, M.; Jeong, J. − R.; Hwang, I. − W.; Song, M. H.; Kim, B. − S.; Kim, J. Y. Versatile Surface Plasmon Resonance of Carbon-dot-supported Silver Nanoparticles in Polymer Optoelectronic Devices. *Nat. Photonics* **2013**, *7*, 732−738.
(9) Lu, L.; Chen, W.; Xu, T.; Yu, L. High-Performance Ternary Blend Polymer Solar Cells involving both Energy Transfer and Hole Relay Processes. *Nat. Commun.* **2015**, *6*, 7327.
(10) Yusoff, A. R. b M.; Kim, D.; Kim, H. P.; Shneider, F. K.; Silva, W. J.; Jang, J. A High Efficiency Solution Processed Polymer Inverted Triple-Junction Solar Cell exhibiting A Power Conversion Efficiency of 11.83%. *Energy Environ. Sci.* **2015**, *8*, 303−316.
(11) Chen, J. − D.; Cui, C.; Li, Y. − Q.; Zhou, L.; Ou, Q. − D.; Li, C.; Li, Y.; Tang, J. − X. Single-Junction Polymer Solar Cells Exceeding 10% Power Conversion Efficiency. *Adv. Mater.* **2015**, *27*, 1035−1041.
(12) Ameri, T.; Khoram, P.; Min, J.; Brabec, C. J. Organic Ternary Solar Cells: A Review. *Adv. Mater.* **2013**, *25*, 4245−4266.
(13) Lu, L.; Xu, T.; Chen, W.; Landry, E. S.; Yu, L. Ternary Blend Polymer Solar Cells with Enhanced Power Conversion Efficiency. *Nat. Photonics* **2014**, *8*, 716−722.
(14) Zhang, Y.; Deng, D.; Lu, K.; Zhang, J.; Xia, B.; Zhao, Y.; Fang, J.; Wei, Z. Synergistic Effect of Polymer and Small Molecules for High-Performance Ternary Organic Solar Cells. *Adv. Mater.* **2015**, *27*, 1071−1076.
(15) Yang, Y.; Chen, W.; Dou, L.; Chang, W. − H.; Duan, H. − S.; Bob, B.; Li, G.; Yang, Y. High-Performance Multiple-Donor Bulk Heterojunction Solar Cells. *Nat. Photonics* **2015**, *9*, 190−198.
(16) Ye, L.; Xu, H. − H.; Yu, H.; Xu, W. − Y.; Li, H.; Wang, H.; Zhao, N.; Xu, J. − B. Ternary Bulk Heterojunction Photovoltaic Cells Composed of Small Molecule Donor Additive as Cascade Material. *J. Phys. Chem. C* **2014**, *118*, 20094−20099.
(17) Khlyabich, P. P.; Burkhart, B.; Thompson, B. C. Efficient Ternary Blend Bulk Heterojunction Solar Cells with Tunable Open-Circuit Voltage. *J. Am. Chem. Soc.* **2011**, *133*, 14534−14537.
(18) Ko, S. − J.; Lee, W.; Choi, H.; Walker, B.; Yum, S.; Kim, S.; Shin, T. J.; Woo, H. Y.; Kim, J. Y. Improved Performance in Polymer Solar Cells Using Mixed $PC_{61}BM/PC_{71}BM$ Acceptors. *Adv. Energy Mater.* **2015**, *5*, 1401687.
(19) Huang, T. − Y.; Patra, D.; Hsiao, Y. − S.; Chang, S. H.; Wu, C. − G.; Ho, K. − C.; Chu, C. − W. Efficient Ternary Bulk Heterojunction Solar Cells Based on Small Molecules Only. *J. Mater. Chem. A* **2015**, *3*, 10512−10518.
(20) Moulé, A. J.; Meerholz, K. Morphology Control in Solution-Processed Bulk-Heterojunction Solar Cell Mixtures. *Adv. Funct. Mater.* **2009**, *19*, 3028−3036.
(21) Huang, Y.; Kramer, E. J.; Heeger, A. J.; Bazan, G. C. Bulk Heterojunction Solar Cells: Morphology and Performance Relationships. *Chem. Rev.* **2014**, *114*, 7006−7043.
(22) Zhou, J.; Zuo, Y.; Wan, X.; Long, G.; Zhang, Q.; Ni, W.; Liu, Y.; Li, Z.; He, G.; Li, C.; Kan, B.; Li, M.; Chen, Y. Solution-Processed and High-Performance Organic Solar Cells Using Small Molecules with a Benzodithiophene Unit. *J. Am. Chem. Soc.* **2013**, *135*, 8484−8487.
(23) He, Z.; Zhong, C.; Su, S.; Xu, M.; Wu, H.; Cao, Y. Enhanced Power-Conversion Efficiency in Polymer Solar Cells using An Inverted Device Structure. *Nat. Photonics* **2012**, *6*, 593−595.
(24) Thompson, B. C.; Fréchet, J. M. J. Polymer-Fullerene Composite Solar Cells. *Angew. Chem., Int. Ed.* **2008**, *47*, 58−77.
(25) He, Y.; Chen, H. Y.; Hou, J.; Li, Y. Indene-C(60) bisadduct: A New Acceptor for High-Performance Polymer Solar Cells. *J. Am. Chem. Soc.* **2010**, *132*, 1377−1382.
(26) Lu, L.; Xu, T.; Chen, W.; Landry, E. S.; Yu, L. Ternary Blend Polymer Solar Cells with Enhanced Power Conversion Efficiency. *Nat. Photonics* **2014**, *8*, 716−722.
(27) Peet, J.; Kim, J. Y.; Coates, N. E.; Ma, W. L.; Moses, D.; Heeger, A. J.; Bazan, G. C. Efficiency Enhancement in Low-Bandgap Polymer Solar Cells by Processing with Alkane Dithiols. *Nat. Mater.* **2007**, *6*, 497−500.
(28) Veerender, P.; Saxena, V.; Chauhan, A. K.; Koiry, S. P.; Jha, P.; Gusain, A.; Choudhury, S.; Aswal, D. K.; Gupta, S. K. Probing the Annealing Induced Molecular Ordering in Bulk Heterojunction Polymer Solar Cells using In-Situ Raman Spectroscopy. *Sol. Energy Mater. Sol. Cells* **2014**, *120*, 526−535.
(29) Congreve, D. N.; Lee, J.; Thompson, N. J.; Hontz, E.; Yost, S. R.; Reusswig, P. D.; Bahlke, M. E.; Reineke, S.; Voorhis, T. V.; Baldo, M. A. External Quantum Efficiency Above 100% in a Singlet-Exciton-Fission-Based Organic Photovoltaic Cell. *Science* **2013**, *340*, 334−337.
(30) Bartelt, J. A.; Lam, D.; Burke, T. M.; Sweetnam, S. M.; McGehee, M. D. Charge-Carrier Mobility Requirements for Bulk Heterojunction Solar Cells with High Fill Factor and External Quantum Efficiency > 90%. *Adv. Energy Mater.* **2015**, *5*, 1500577 (Early view, DOI: 10.1002/aenm.201500577)..
(31) Sharenko, A.; Kuik, M.; Toney, M. F.; Nguyen, T. − Q. Crystallization-Induced Phase Separation in Solution-Processed Small Molecule Bulk Heterojunction Organic Solar Cells. *Adv. Funct. Mater.* **2014**, *24*, 3543−3550.
(32) Huang, W.; Gann, E.; Thomsen, L.; Dong, C.; Cheng, Y. − B.; McNeill, C. R. Unraveling the Morphology of High Efficiency Polymer Solar Cells Based on the Donor Polymer PBDTTT-EFT. *Adv. Energy Mater.* **2015**, *5*, 1401259.
(33) Savagatrup, S.; Printz, A. D.; O'Connor, T. F.; Zaretski, A. V.; Rodriquez, D.; Sawyer, E. J.; Rajan, K. M.; Acosta, R. I.; Root, S. E.; Lipomi, D. J. Mechanical Degradation and Stability of Organic Solar Cells: Molecular and Microstructrual Determinants. *Energy Environ. Sci.* **2015**, *8*, 55−80.
(34) Gao, J.; Chen, W.; Dou, L.; Chen, C. − C.; Chang, W. − H.; Liu, Y.; Li, G.; Yang, Y. Elucidating Double Aggregation Mechanisms in the Mophology Optimization of Diketopyrrolopyrrole-Based Narrow Bandgap Polymer Solar Cells. *Adv. Mater.* **2014**, *26*, 3142−3147.
(35) Müller-Buschbaum, P. The Active Layer Morphology of Organic Solar Cells Probed with Grazing Incidence Scattering Techniques. *Adv. Mater.* **2014**, *26*, 7692−7709.
(36) Gao, J.; Dou, L.; Chen, W.; Chen, C. − C.; Guo, X.; You, J.; Bob, B.; Chang, W. − H.; Strzalka, J.; Wang, C.; Li, G.; Yang, Y. Improving Structural Order for a High-Performance Diketopyrrolopyrrole-Based Polymer Solar Cells with a Thick Active Layer. *Adv. Energy Mater.* **2014**, *4*, 1300739.

DOI: 10.1021/acsami.5b06365
ACS Appl. Mater. Interfaces 2015, 7, 21423−21432

(37) Awartani, O.; Kudenov, M. W.; Kline, R. J.; O'Connor, B. T. In-Plane Alignment in Organic Solar Cells to Probe the Morphological Dependence of Charge Recombination. *Adv. Funct. Mater.* **2015**, *25*, 1296−1303.
(38) Kim, Y. J.; Chung, D. S.; Park, C. E. Highly Thermally Stable Non-fullerene Organic Solar Cells: p-DTS(FBTTh$_2$)$_2$:P(NDI2OD-T2) Bulk Heterojunction. *Nano Energy* **2015**, *15*, 343−352.
(39) Huang, Y.; Wen, W.; Mukherjee, S.; Ade, H.; Kramer, E. J.; Bazan, G. C. High-Molecular-Weight Insulating Polymers Can Improve the Performance of Molecular Solar Cells. *Adv. Mater.* **2014**, *26*, 4168−4172.
(40) Proctor, C. M.; Love, J. A.; Nguyen, T. − Q. Mobility Guidelines for High Fill Factor Solution-Processed Small Molecule Solar Cells. *Adv. Mater.* **2014**, *26*, 5957−5961.
(41) Cowan, S. R.; Street, R. A.; Cho, S.; Heeger, A. J. Transient Photoconductivity in Polymer Bulk Heterojunction Solar Cells: Competition Between Sweep-Out and Recombination. *Phys. Rev. B: Condens. Matter Mater. Phys.* **2011**, *83*, 035205.
(42) Koster, L. J. A.; Smits, E. C. P.; Mihailetchi, V. D.; Blom, P. W. M. Device Model for The Operation of Polymer/Fullerene Bulk Heterojunction Solar Cells. *Phys. Rev. B: Condens. Matter Mater. Phys.* **2005**, *72*, 085205.
(43) Blom, P. W. M.; Mihailetchi, V. D.; Koster, L. J. A.; Markov, D. E. Device Physics of Polymer:Fullerene Bulk Heterojunction Solar Cells. *Adv. Mater.* **2007**, *19*, 1551−1566.
(44) Huang, D.; Li, Y.; Xu, Z.; Zhao, S.; Zhao, L.; Zhao, J. Enhanced Performance and Morphological Evolution of PTB7:PC$_{71}$BM Polymer Solar Cells by Using Solvent Mixtures with Different Additives. *Phys. Chem. Chem. Phys.* **2015**, *17*, 8053−8060.
(45) Zhao, J.; Li, Y.; Lin, H.; Liu, Y.; Jiang, K.; Mu, C.; Ma, T.; Lai, J.; Hu, H.; Yu, D.; Yan, H. High-Efficiency Non-Fullerene Organic Solar Cells Enabled by a Difluorobenzothiadiazole-Based Donor Polymer Combined with A Properly Matched Small Molecule Acceptor. *Energy Environ. Sci.* **2015**, *8*, 520−525.
(46) Mihailetchi, V. D.; Koster, L. J. A.; Blom, P. W. M.; Melzer, C.; Boer, B.; Duren, J. K. J.; Janssen, R. A. J. Compositional Dependence of the Performance of Poly(*p*-phenylenevinylene):Methanofullerene Bulk-Heterojunction Solar Cells. *Adv. Funct. Mater.* **2005**, *15*, 795−801.
(47) Proctor, C. M.; Nguyen, T. − Q. Effect of Leakage Current and Shunt Resistance on The Light Intensity Dependence of Organic Solar Cells. *Appl. Phys. Lett.* **2015**, *106*, 083301.
(48) Koster, L. J. A.; Mihailetchi, V. D.; Xie, H.; Blom, P. W. M. Origin of the Light Intensity Dependence of the Short-Circuit Current of Polymer/Fullerene Solar Cells. *Appl. Phys. Lett.* **2005**, *87*, 203502.
(49) Rand, B. P.; Burk, D. P.; Forrest, S. R. Offset Energies at Organic Semiconductor Heterojunctions and Their influence on the Open-Circuit Voltage of Thin-Film Solar Cells. *Phys. Rev. B: Condens. Matter Mater. Phys.* **2007**, *75*, 115327.
(50) Staple, D. B.; Oliver, P. A. K.; Hill, I. G. Derivation of The Open-Circuit Voltage of Organic Solar Cells. *Phys. Rev. B: Condens. Matter Mater. Phys.* **2014**, *89*, 205313.

DOI: 10.1021/acsami.5b06365
ACS Appl. Mater. Interfaces 2015, 7, 21423−21432